

Three-dimensional grain fabric measurements using high-resolution X-ray computed tomography

Richard A. Ketcham*

Jackson School of Geosciences, The University of Texas at Austin, Austin, TX 78712, USA

Received in revised form 12 February 2004

Accepted 3 February 2005
Available online 6 July 2005

Abstract

High-resolution X-ray computed tomography (HRXCT) provides detailed imagery of the interiors of rocks up to hand-sample size, non-destructively and in three dimensions. New tools described here allow these data to be used for analysis of grain fabrics. Two separate sets of measurement techniques have been developed. The first concentrates on quantifying individual crystals (phenocrysts, porphyroblasts) or other discrete objects or void spaces within a sample. Quantifiable properties include location, size, shape, orientation, and contact relationships with adjacent objects. The second set of techniques performs a more general fabric analysis on any distinguishable component in a sample. A fabric tensor can be computed based on a number of metrics, including the star volume distribution (SVD), star length distribution (SLD), and mean intercept length (MIL) methods. The fabric tensors provide principal component directions and magnitudes, which in turn provide a measure of degree of anisotropy and shape indices. Because the SVD and SLD measure only the material of interest, whereas the MIL is also influenced by spatial distribution, results can be divergent for sparse phases. Also introduced is a three-dimensional rose diagram that can be viewed interactively and inspected to reveal further details about non-orthogonal directional components. These techniques are demonstrated through analysis of a garnet–kyanite schist from Mica Dam, British Columbia.

© 2005 Elsevier Ltd. All rights reserved.

Keywords: Fabric analysis; Computed tomography; Intercept methods; Preferred orientations; Contact normals

1. Introduction

Quantification of textural features defined by grain shape and shape preferred orientation (SPO) has generally relied on processing of two-dimensional images, such as photographs, micrographs, and acetate peels. Available analytical approaches include manual measurement of image features (Shimamoto and Ikeda, 1976; Panozzo, 1983), intercept counting methods (Rink, 1976; Launeau and Robin, 1996) and autocorrelation (Panozzo Heilbronner, 1992). These measurements provide two-dimensional information, and if analyses are obtained on multiple planes then three-dimensional strain can be calculated using stereological methods (Grégoire et al., 1998). A potential drawback to

these tools is that they are somewhat destructive, usually requiring at least the excision of two-dimensional samples from a three-dimensional specimen. They can also be susceptible to sample inhomogeneity, insofar as different observation planes must come from different parts of a specimen.

This paper introduces high-resolution X-ray computed tomography (HRXCT) as a new tool for fabric analysis that overcomes these limitations by nondestructively providing three-dimensional (3D) data describing an entire sample volume. These data may be visualized as a powerful tool to aid in petrographic observation, and are amenable to many of the quantitative approaches used for two-dimensional data, which are now directly implemented and applied in 3D.

1.1. High-resolution X-ray CT

HRXCT is based on the same principles as medical CAT (computed axial tomography) scanning. In its simplest

* Tel.: +1 512 471 6942; fax: +1 512 471 9425.
E-mail address: ketcham@mail.utexas.edu.

form, an X-ray fan beam is directed at an object from all orientations in a plane, and the decrease in X-ray intensity caused by passage through the object is measured by a linear array of detectors (Fig. 1). The resulting data are then reconstructed to create a cross-sectional image of the object along that plane (e.g. Fig. 2). The grayscales in such images reflect the relative linear X-ray attenuation coefficient (μ), which is a function of density, atomic number, and X-ray energy. Each CT (computed tomography or computed tomographic) image is termed a ‘slice’, as it corresponds to what one would see if the object were sliced open along the scan plane. By gathering a stack of contiguous slices, data for a complete 3D volume can be obtained. Because each slice represents a finite thickness of material, corresponding to the thickness of the collimated X-ray beam and detector array, the pixels in CT images are referred to as voxels (volume elements). A more detailed summary of CT and its application to geological materials is provided by Ketcham and Carlson (2001).

Originally developed for industrial applications, HRXCT differs from medical scanning by taking advantage of the fact that the scan subject is not alive, and thus does not move and is not harmed by X-rays. This allows use of higher-energy X-rays and longer dosage times, along with smaller detectors and more precise positioning. When combined, these factors give HRXCT 1–3 orders of magnitude better resolution than medical scanners, and allow higher-density objects to be imaged successfully (Ketcham and Carlson, 2001). At the same time, the technique is entirely nondestructive, leaving samples available for other analyses after scanning.

A number of useful textural measurements have been extracted from HRXCT data, including crystal size and location (Carlson and Denison, 1992; Denison and Carlson, 1997; Denison et al., 1997; Hirsch et al., 2000), vesicle size distribution (Sahagian et al., 2002), and modal percentages (Brown et al., 1999; Philpotts et al., 1999; Koeberl et al., 2002). HRXCT has also been used to quantify the

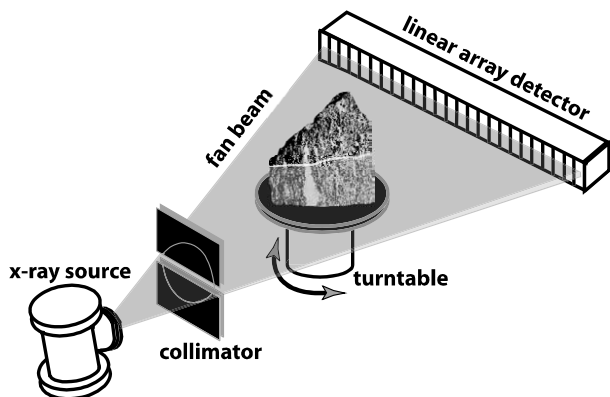


Fig. 1. Schematic illustration of X-ray CT. A collimated planar X-ray fan beam is directed at the sample and readings are taken on a linear detector array at constant-angle intervals through a full rotation. The resulting data are used to reconstruct a sample cross-section along the slice plane (Fig. 2).

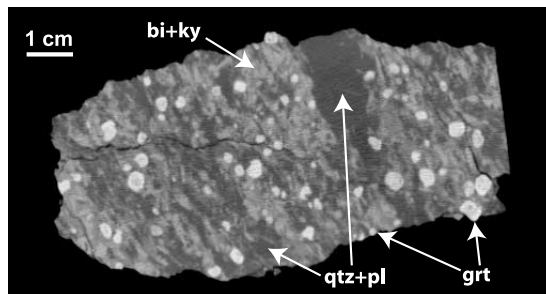


Fig. 2. Example HRXCT slice of garnet–kyanite schist MD from Mica Dam, British Columbia. Increasing brightness reflects relative X-ray attenuation in a 0.5-mm-thick slice of the sample. The darkest material is quartz and plagioclase, followed in ascending brightness order by biotite, kyanite, and garnet.

orientation and anisotropy in cancellous bone (Fajardo and Müller, 2001; Ryan and Ketcham, 2002). The principal impediments to quantitative analysis from HRXCT imagery to date have been that the data sets are large (100's–1000's of Mb) and difficult to work with, and few software tools have been available that are able to efficiently deal with the vagaries of CT data and extract measurements of interest. This paper introduces tools that have been developed to overcome these impediments and help facilitate more routine utilization of HRXCT and other three-dimensional imagery for textural analysis.

2. Data

2.1. Specimen

Specimen MD is a 12 cm × 11 cm × 5 cm sample of schist from the Mica Creek locality near Mica Dam, British Columbia, featuring almandine garnets in a foliated, coarse-grained matrix of muscovite, biotite, kyanite, plagioclase and quartz. The Mica Dam area features at least three sets of fold structures, each of which has an associated axial-planar foliation (Simony et al., 1980). The principal overt structural feature in sample MD is the early schistosity (S_{1+2}) defined by aligned kyanite and biotite, which was deformed in the final stages of folding; metamorphic minerals are deformed by S_3 crenulations, indicating that final stage of deformation post-dated the metamorphic climax. Inclusion trails in garnet are discordant to the S_{1+2} schistosity, indicating at least some garnet growth predated S_{1+2} (Crowley et al., 2000). A compositional microprobe map of a large garnet from this locality shows strongly elliptical zoning aligned with inclusions oblique to the surrounding foliation (Tinkham and Ghent, 2003), suggesting that early garnet growth may have been ellipsoidal. The sample was included in previous studies of metamorphic textures that utilized CT to quantify the spatial distribution of porphyroblasts (Carlson and Denison,

1992; Denison and Carlson, 1997). Newer and better-resolution scan data were acquired for this study.

2.2. CT data

The sample was scanned at the High-resolution X-ray CT Facility at the University of Texas (UTCT), which is described in detail by Ketcham and Carlson (2001). Two subsystems are used to image geological specimens across a range of size classes. The high-resolution subsystem uses a 420 kV X-ray source and a pair of linear array detectors to image samples from 50–500 mm in diameter, with slice thicknesses down to 0.25 mm. The ultra-high-resolution subsystem uses a 200 kV microfocal X-ray source with an image intensifier detector sampled by a 1024 × 1024 CCD video camera to image samples from 3 to 70 mm in diameter at slice thicknesses down to 10's or even 1's of micrometers. Both X-ray sources are polychromatic, producing X-rays over a continuum of energies from about 30 keV up to their operating voltage (i.e. up to 420 keV for the 420 kV source).

Because of its large size sample, MD was scanned on the high-resolution subsystem. The sample was scanned at 420 kV and 4.7 mA using a second-generation (translate-rotate) scanning protocol (Ketcham and Carlson, 2001). A total of 240 images were obtained with a slice spacing of 0.5 mm and a pixel spacing of 0.25 mm. A representative CT slice is shown in Fig. 2.

Resolution for CT systems is defined to first order by the dimensions of the data voxels. The z dimension corresponds to the spacing between slice planes, which is usually equal to or slightly below the slice thickness. The x – y resolution is typically the sample cross-sectional diameter divided by the image pixel dimension, usually 512 or 1024 depending primarily on the number of detector channels and geometric factors. To be resolved, a feature within the sample volume must typically span several voxels in at least one dimension, and more favorably in two or three. For example, a spherical mineral grain having moderate contrast with the surrounding matrix may need to be approximately 3 voxel widths in diameter to be confidently identified and measured, while a fracture may be detectable even if it is less than one voxel wide by extending several voxels in its other two dimensions.

The degree to which different components within a rock volume can be distinguished in HRXCT data depends on the difference in their linear attenuation coefficients. The equation describing X-ray attenuation is:

$$I = I_0 \exp(-\mu x),$$

where I_0 is the initial intensity of an X-ray beam and I is the intensity after it has passed through a thickness x of material with attenuation coefficient μ . Example μ values for minerals observed in sample MD over the range of X-ray energies generated by the 420 kV source are shown in Fig. 3. At energies below 100–150 keV the dominant

attenuation mechanism is photoelectric absorption, which is primarily controlled by effective atomic number Z , varying roughly as a factor of $Z^{3.8}/E^{3.2}$ (McCullough, 1975), where E is X-ray energy in keV. At higher energies Compton scattering predominates, which is controlled mainly by density, as it varies roughly linearly with Z . Attenuation coefficients can be estimated using published tables (e.g. Markowicz, 1993), but the best source is the XCOM Photon Cross-Sections Database provided on-line by the National Institute of Standards and Technology (<http://physics.nist.gov/PhysRefData/Xcom/Text/XCOM.html>). The XCOM database calculates mass attenuation coefficients, which are converted to linear attenuation coefficients by multiplying by density.

The contrast between attenuation mechanisms is particularly apparent when comparing the curves for biotite and kyanite: the iron and magnesium in biotite gives it higher attenuation at low energies, while the higher density of kyanite (3.6 g/cm³ vs. 3.0 g/cm³) makes it more attenuating to higher-energy X-rays. Although the peak X-ray energy used was 420 keV, the weighted mean X-ray energy of the polychromatic beam was closer to 125 keV, making these two phases hard to distinguish, as reflected in Fig. 2. If distinguishing kyanite from biotite were a study requirement, restricting the X-ray energy spectrum to values above or below their crossover point would improve contrast. Each option involves trade-offs, however. Low-energy X-rays can be preferentially filtered out by passing the beam through a high- Z material (typically a copper or brass plate), but this also degrades the high-energy X-ray signal somewhat, resulting in greater image noise. Scanning at exclusively low energies is restricted by the lower penetrating ability of the X-rays, decreasing the volume of rock that can be imaged. Another approach would be to scan the sample twice at different energies to help separate the effects of density versus atomic number (e.g. Van Geet et al., 2000). It is also important to note that the curves in Fig. 3 are idealizations based on pure crystalline material. To the extent that rock materials contain impurities, zoning, porosity, or alteration, their true attenuation can vary significantly, causing difficulties in reliable identification and separation of phases.

3. Analysis methods

Data investigation often begins with visualization, as it will provide information for subsequent analysis and can in and of itself provide useful insights. The first step in quantitative analysis is segmentation, or identification of which voxels or regions within the sample correspond to which materials. In cases where the phase of interest is clearly identifiable from the rest of the specimen this step can be trivial (such as a gray level threshold), but many situations require additional image processing. Following segmentation, two approaches for textural analysis are

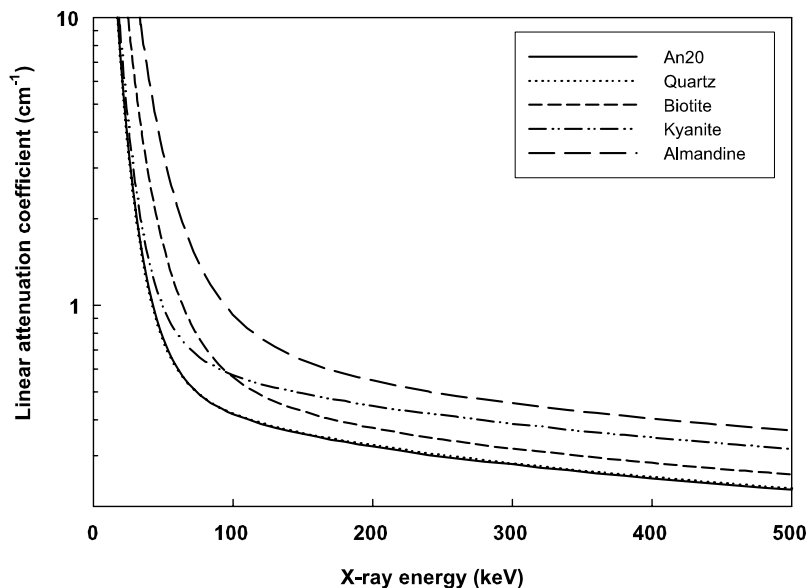


Fig. 3. Linear attenuation coefficients for principal minerals in sample MD. Grayscale in CT images reflect linear attenuation coefficient, which is a function of density, atomic number and X-ray energy. The values shown here are based on end-member compositions and densities, and were calculated using the XCOM Photon Cross-Sections Database (<http://physics.nist.gov/PhysRefData/Xcom/Text/XCOM.html>).

available. The object-based approach seeks to identify and isolate each distinct object of interest in the data volume, which then allows measurement of these objects and their interrelationships. The fabric-based approach quantifies the orientation and degree of anisotropy within each material of interest.

3.1. Visualization

A CT data set can be visualized using a variety of techniques to reveal textural features. One straightforward method is to view the slice data, either individually or as an animation through an entire data set. The data can also be resampled along orthogonal or oblique planes to allow viewing along different orientations. The most powerful three-dimensional visualization technique is volume rendering (Fig. 4), in which each grayscale value in the data set is assigned a color and an opacity value. This allows some phases to be rendered transparent and others partially or entirely opaque, providing unique opportunities for petrographic analysis in three dimensions. A number of commercial software packages implement volume rendering.

3.2. Segmentation

The simplest segmentation method for CT data is to define a grayscale threshold or range that is unique to the phase of interest. However, this approach is complicated by the finite resolution of the imagery. Because each data voxel encompasses a volume of material, if more than one material is present in that volume, the resulting CT

grayscale will be some average of the phases present; this is known as the partial volume effect. Furthermore, some blurring is inevitable, causing the grayscale value within a voxel to be influenced by surrounding material. Thus material boundaries, rather than being sharp, will often extend across 2–4 voxel widths featuring a gradual grayscale transition between the end-member values characterizing each phase.

The grayscale level for proper location of a boundary between two different materials is the mean of their end-member values. For the MD scan data, the mean end-member grayscale for garnet was 240, while biotite and kyanite had a mean value of about 198 and quartz and plagioclase had a mean value of 160. Because garnet is most frequently in contact with quartz and plagioclase, an appropriate threshold value is 200; however, globally, thresholding with this value would include many biotite and kyanite voxels. To achieve a proper segmentation, a sequential neighborhood-based algorithm that takes connectivity into account is used, selecting only those low-grayscale voxels that are in close proximity to voxels interior to garnets and thus have unambiguously high values. A three-step process was used: first, the set of voxels with values ≥ 218 was found; second, all voxels ≥ 212 and connected to first-set voxels by a 3D path of any length were selected; finally, all voxels ≥ 200 and in immediate contact with a first- or second-set voxel were added. Segmentation of a multi-phase rock proceeds sequentially, generally from brightest phase to darkest (or vice versa, if vesicle or pore space is being examined), setting aside voxels as they are selected so they are not reassigned during subsequent segmentations.

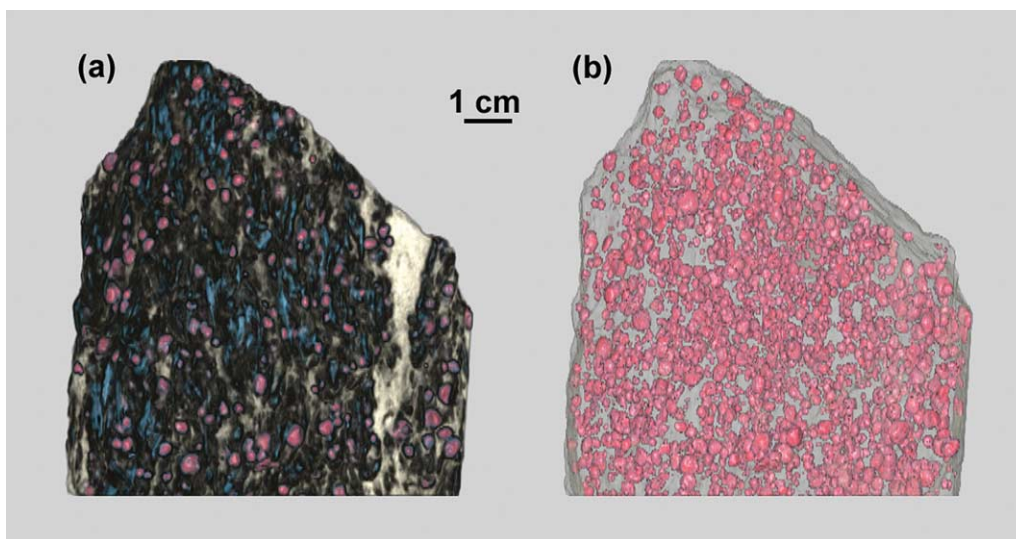


Fig. 4. Three-dimensional reconstructions of HRXCT data; the slice plane shown in Fig. 2 corresponds to a horizontal slice through these renderings. The renderings are created by compiling all of the CT slice images into a 3D volume, and assigning each data voxel a color and opacity. In (a), colors have been chosen to roughly replicate the actual rock, with quartz and plagioclase in white, garnet in red, and kyanite and biotite in blue and black. In (b), all but garnet has been rendered transparent, allowing garnets internal to the sample to be seen.

3.3. Object-based analysis

The software developed for object-based analysis is called BLOB3D (Ketcham in press), as it implements a three-dimensional extension of the standard 2D image processing technique of blob analysis, in which contiguous regions of pixels ('blobs') are identified and measured. BLOB3D is organized into three modules, which divide the problem into its component parts, SEGMENT, SEPARATE, and EXTRACT. The SEGMENT module executes the segmentation step, an example of which is discussed above. The SEPARATE module scans the data volume to find sets of voxels that are connected in 3D. Each set may represent a single object, or a cluster of objects that are touching or inter-grown. In the latter case the blob can be cut apart to separate the component objects from each other using a set of manual and semi-automated three-dimensional editing tools. Once all objects have been separated, the EXTRACT module calculates measurements of interest, such as location, volume, shape, orientation, and contact relationships. The most time-consuming step is SEPARATE, as each choice of how to cut objects apart is made by the program operator. An experienced operator will take on average a few seconds per object separated. Fig. 5 shows an example of BLOB3D analysis for sample MD.

3.4. Fabric analysis

Grain-shape fabric analysis is carried out using a program called QUANT3D, which is described in detail by Ketcham and Ryan (2004). The complete volumetric coverage provided by CT data provides an ideal setting for performing oriented measurements that characterize various aspects of grain shape. A number of measurement

methodologies are available, including the star volume distribution (SVD) (Cruz-Orive et al., 1992; Karlsson and Cruz-Orive, 1993), star length distribution (SLD) (Odgaard et al., 1997; Smit et al., 1998), and mean intercept length (MIL) (Cowin, 1986; Harrigan and Mann, 1984; Launeau and Robin, 1996; Whitehouse, 1974). The 'star' methods are calculated by placing a series of points within the material of interest and measuring the lengths of lines emanating from them in various directions until they encounter a boundary (Fig. 6a). For the SVD, these lines are considered infinitesimal cones, with their vertex at the origin point and subtending a solid angle as they approach the material interface. The star volume component \bar{v}_V^* for direction ω is defined:

$$\bar{v}_V^*(\omega) = \frac{\pi}{3n} \sum_{i=1}^n L_i^3(\omega) \quad (1)$$

where n is the number of points used and L_i is the length of the line passing through point i with orientation ω that stays entirely within the material of interest. The star volume from a particular point within an object is the star volume component summed over all orientations. By this definition, the star volume of a convex object is equal to its standard volume, whereas for a more irregular object the star volume is the volume that can be 'seen' from the test point. For the star length component s the lines remain as lines:

$$s(\omega) = \frac{1}{n} \sum_{i=1}^n L_i(\omega). \quad (2)$$

The MIL method is similar to the SVD and SLD, only the linear traverses are extended to cross multiple material boundaries. A series of traverses is made, along which all material intersections are located and the distances between

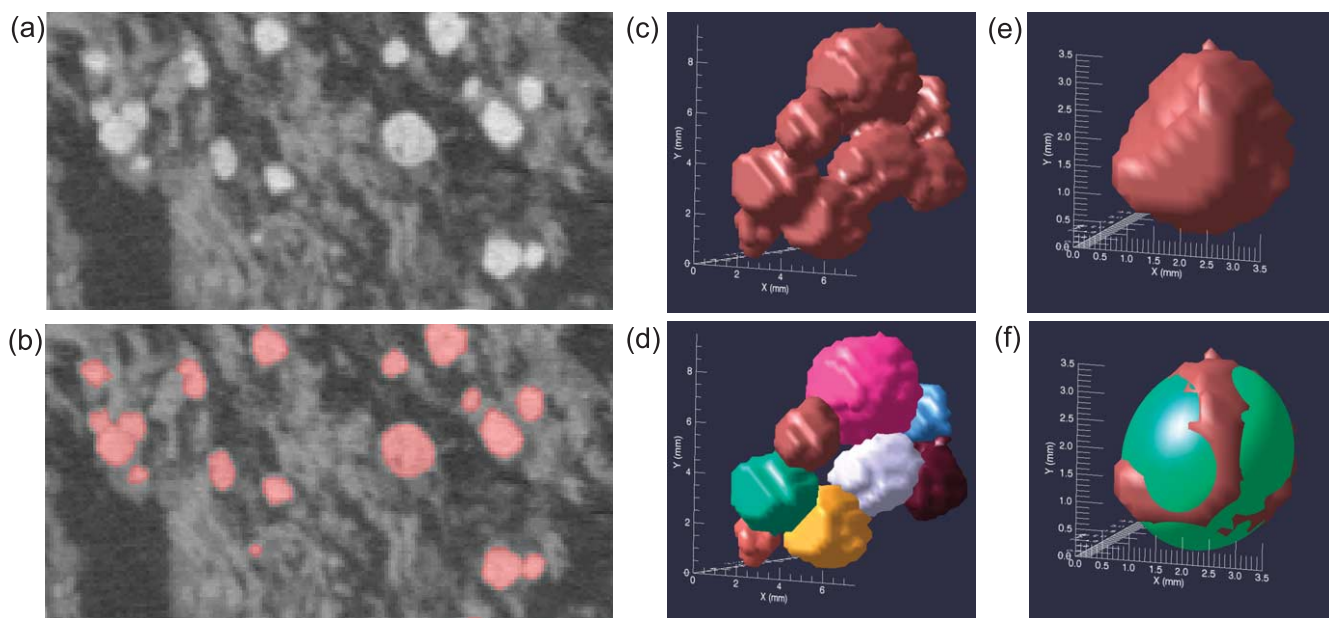


Fig. 5. Examples from the three modules of BLOB3D. SEGMENT (left): (a) shows a part of MD CT scan data, and (b) shows segmentation of garnet; horizontal field is 4.5 cm. SEPARATE (center): (c) shows a 3D rendering of the cluster of garnets that includes the trio of touching garnets on the left side of (a) and (b) as the lower-left three (they are upside down in this view). Touching and impinging garnets are separated (d) by the program operator using manual and semi-automated tools. EXTRACT (right): a variety of quantitative data can be obtained. In (e), the outer surface of the yellow garnet from (d) is fitted with an ellipsoid (f) to determine orientation and shape anisotropy.

them measured (Launeau and Robin, 1996). The MIL component for an orientation ω is the mean length between intercepts along all traverses in that direction. Because MIL traverses cross multiple boundaries, they reflect features of both the material of interest and the surrounding material, and in fact the MIL is identical for any image and its inverse. The star analyses, on the other hand, reflect only the material of interest.

All these measurements are made using an algorithm that traverses the voxel grid in an arbitrary 3D orientation and tests for material intersections. The algorithm in QUANT3D includes a renormalization that compensates for the biasing effects of cubic and non-equidimensional voxels (Ketcham and Ryan, 2004). The set of orientations for an analysis may be randomly generated, but a better solution is to use a regular distribution that is close to uniformly distributed on a sphere (Fig. 6b). A faceted grid is created by recursively subdividing the faces of an octahedron and projecting all vertices outward to the surface of a unit sphere. Each vector from the origin a vertex corresponds to an analysis direction.

There are two approaches to summarizing SVD, SLD, and MIL measurements. First, a *fabric tensor* may be used, akin to a stress or strain tensor, which describes how the moment of inertia of a particular quantity varies with orientation (see Appendix A). The fabric tensor eigenvectors \hat{u}_1 , \hat{u}_2 , \hat{u}_3 and eigenvalues $\hat{\tau}_1$, $\hat{\tau}_2$, $\hat{\tau}_3$ define orthogonal principal axes, with \hat{u}_1 and \hat{u}_3 corresponding to the axes along which the moment of inertia is minimized and maximized, respectively. The eigenvalues are related to the moment of inertia about each axis (see Appendix A).

Standard summaries of the eigenvalues are the degree of anisotropy DA ($\hat{\tau}_1/\hat{\tau}_3$), as well as the shape parameters of Benn (1994): the isotropy index I ($\hat{\tau}_3/\hat{\tau}_1$) and the elongation index E ($1 - (\hat{\tau}_2/\hat{\tau}_1)$).

Second, the data can be visualized, either with a standard stereonet or by using a three-dimensional version of a rose diagram (Fig. 6c). A 3D rose diagram is created by projecting each analysis direction vertex from the unit sphere inward or outward from the origin according to its corresponding star component or MIL measurement. Vertex positions and colors are normalized by dividing by the maximum measurement value. A normalized value of 1.0 plots in red at a distance from the origin equal to the coordinate axis length, and lower values plot in successively ‘cooler’ rainbow colors and proportionally closer to the origin. This coloring convention allows the relative measurement values to be easily ascertained; for example, the appearance of dark blue indicates that there is a roughly factor 10 difference between the minimum and maximum measurements. Also plotted on these diagrams are the eigenvector directions, with axis lengths scaled by their associated eigenvalues.

The diagrams are best viewed interactively and are exported in VRML format, which is readable by a number of freeware applications and browser plug-ins. While these diagrams do not contain any more information than a standard stereo contour plot, they offer a powerful and novel way of visualizing the data. Among the analyses discussed here, the SVD shows the most contrast and thus potential for visualization. The 3D rose diagram and the fabric tensor are

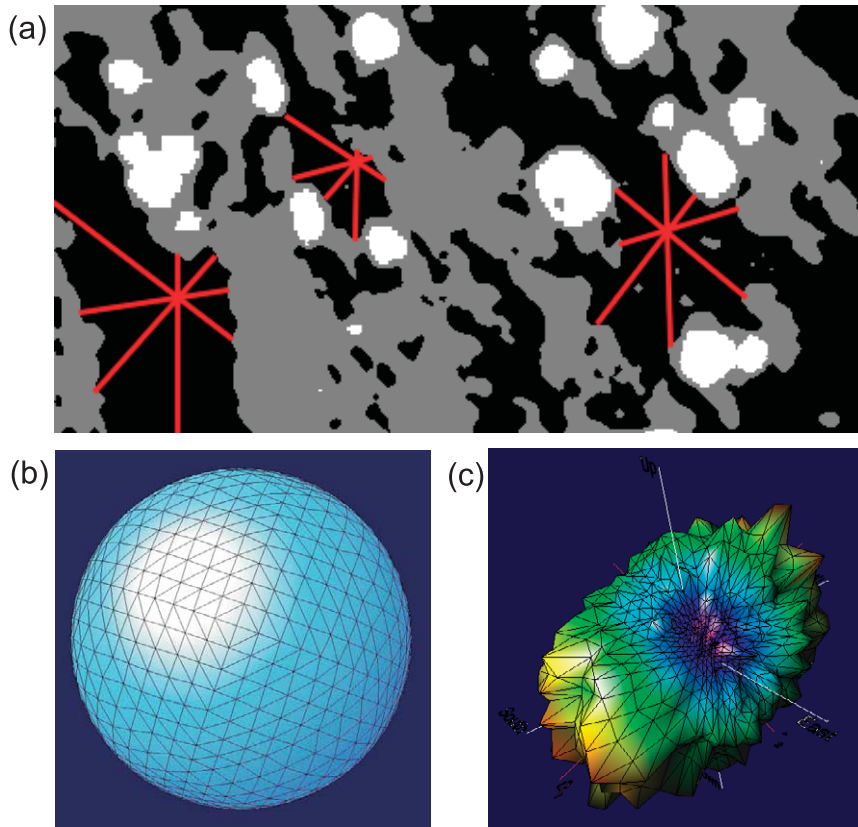


Fig. 6. Example of fabric analysis of quartzofeldspathic layers using QUANT3D. In (a) the scan data (Fig. 5a) are first segmented to isolate the material of interest, in this case garnet (white), biotite+kyanite (gray), and quartz+felspar (black). ‘Star’ analyses proceed by placing a series of points within the material of interest, and measuring the distance from each point to the material boundary in many directions (red lines). Only two dimensions shown here, but measurements are actually made in 3D. The analysis directions (ω_i) are uniformly distributed in three dimensions on a grid defined by the line intersections on the sphere shown in (b). To create a 3D rose diagram, each intersection in (b) is projected from the origin by its relative star volume component value (c). Colors are assigned based on $SVD(\omega_i)/\text{Max}(SVD)$, and color coding from 0 (violet) to 1 (red).

intimately related: the moment of inertia corresponds to the distribution of points in the rose diagram as it is viewed along a particular axis.

4. Analysis and Results

The MD slice data (Fig. 2) can be easily segmented into three components. The brightest is garnet, followed by the biotite–kyanite layers, and the darkest layers are quartz and plagioclase. Garnets are generally subhedral and occasionally impinge one another. Volume rendering of the specimen with all but the garnets transparent (Fig. 4b) shows that the garnets are slightly elongated vertically (normal to the scan plane); this trend is corroborated by observations on the sample surface.

The sample was first processed in BLOB3D to extract the garnets. A total of 3035 garnets were measured, with radii ranging from 0.35 to 3.81 mm. Of these, 2760 were entirely enclosed within the sample volume (i.e. were not on a broken or sawn face) and thus suitable for shape analysis. Three-dimensional grain-shape anisotropy and orientation were measured using best-fit ellipsoids to garnet outer

surfaces. The volume of each crystal was calculated by counting the number of voxels encompassed, from which mean radius was calculated based on a spherical geometry. Examples of plots available from the shape data are shown in Fig. 7. Fig. 7a shows that the garnet porphyroblasts have a positively skewed size distribution typical of many metamorphic rocks (Carlson et al., 1995; Denison and Carlson, 1997). The shape measurements verified and quantified the observed moderate grain-shape anisotropy. The distribution of garnet aspect ratios (Fig. 7b and c) has a consistent base value of about 1.4–1.5 that persists among all size classes, with larger anisotropy values appearing in a subset of smaller classes. Garnet shapes can be summarized with a Flinn plot (Fig. 7d) or a shape diagram (Fig. 7e) after Benn (1994); both plots suggest that departures from sphericity are roughly evenly distributed among rod-like and disc-like shapes.

Orientations based on best-fit ellipsoids can be prone to biasing when a feature subtends relatively few voxels, as there are a limited number of possible configurations. Accordingly, for this study orientations were excluded for crystals with mean diameters of less than 1.5 mm (i.e. 3 voxel long dimensions); 2109 garnets passed this criterion.

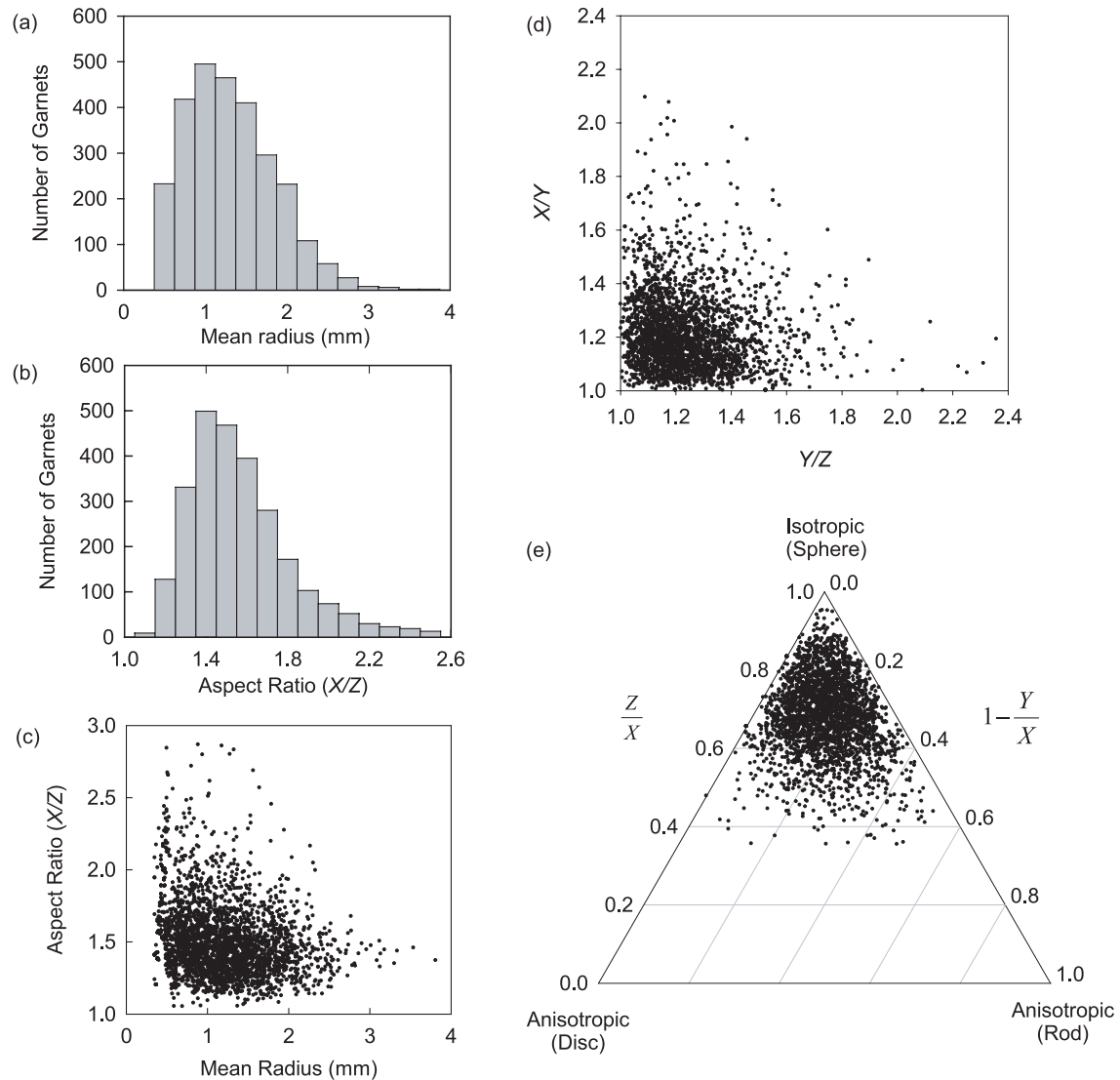


Fig. 7. Analysis of sizes and shapes of 2760 garnets from sample MD using BLOB3D software. Shape measurements based on best-fit ellipsoids for each crystal, giving radii X , Y , and Z from longest to shortest. (a) Size distribution of crystals. (b) Distribution of crystal aspect ratios (long axis/short axis). (c) Relationship of aspect ratio to garnet size. (d) Flinn diagram. (e) Shape diagram after Benn (1994).

Stereo plots of the garnet long axes (Fig. 8a and b) reveal a great circle distribution that parallels the rock foliation (Fig. 2), with a significant vertical peak. Short axes (Fig. 8c and d) are generally normal to the foliation. Eigenvector directions and eigenvalue magnitudes for these distributions are provided in Table 1.

The orientations of garnet–garnet contacts were also measured, by finding the best-fitting plane to the voxel interfaces between touching crystals. A total of 956 contacts were detected, but once again there are biasing effects when contacts have a small surface area, owing to the limited number of possible voxel configurations. In particular,

Table 1
Analysis of garnet orientations from BLOB3D

	Long axes	Short axes	Contact normals
$\hat{\mathbf{u}}_1$	179°/78°	69°/5°	43°/29°
$\hat{\mathbf{u}}_2$	336°/11°	338°/13°	143°/18°
$\hat{\mathbf{u}}_3$	67°/5°	181°/76°	261°/55°
$\hat{\tau}_1$	0.59	0.61	0.45
$\hat{\tau}_2$	0.28	0.25	0.33
$\hat{\tau}_3$	0.14	0.14	0.22

$\hat{\mathbf{u}}_1$, $\hat{\mathbf{u}}_2$, $\hat{\mathbf{u}}_3$, eigenvectors, trend and plunge. $\hat{\tau}_1$, $\hat{\tau}_2$, $\hat{\tau}_3$ = eigenvalues.

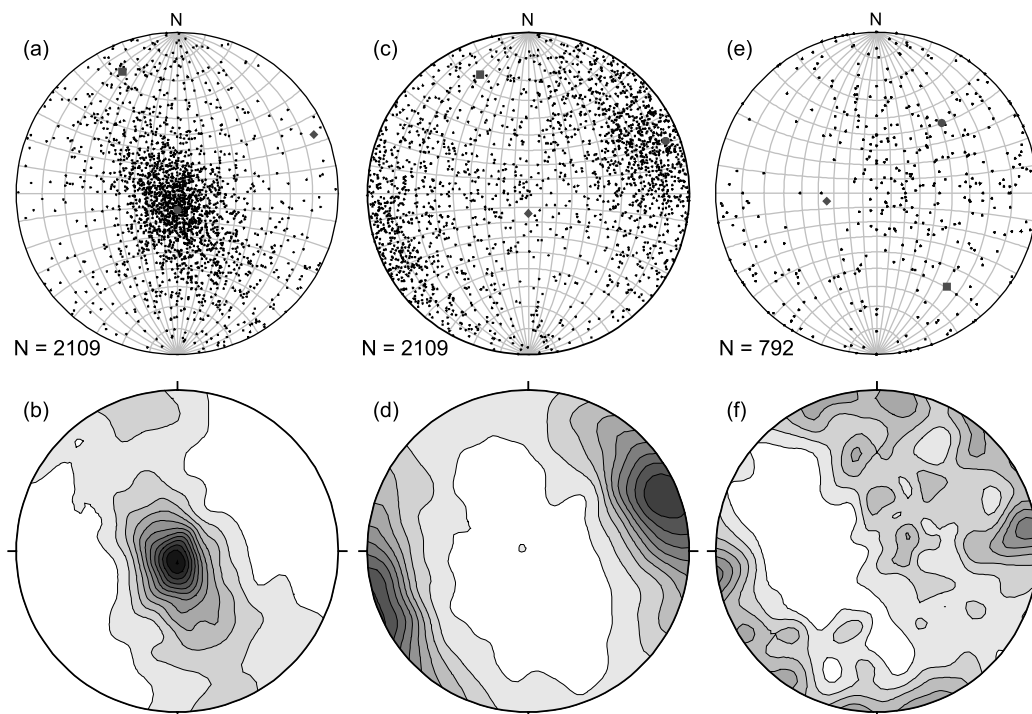


Fig. 8. Stereonet scatterplots and contours diagrams showing orientations of garnet long axes (a,b), garnet short axes (c,d), and normals to best-fit planes to garnet–garnet contacts (e,f), based on BLOB3D analysis. On scatterplots, first, second and third eigenvectors shown by gray circle, triangle, and diamond, respectively. Contours at 0.5 intervals of angle-weighted cosine density, exponent = 99. The sample was not oriented, so directions only refer to the position of the sample in the scanner, not true geographic directions. Plots made using StereoNett software by J. Duyster, Ruhr Universität Bochum, Germany.

orientations normal to voxel faces are heavily favored. Adopting a protocol analogous to that for grain orientations, contacts with surface areas below 1.76 mm^2 (i.e. mean diameters below 1.5 mm) were excluded, leaving a total of 396 contacts. Poles to the contact normal orientations (Fig. 8e and f) show a distinct gap to the southwest of the great circle distribution of long axes.

Robust three-dimensional contact orientation information for particles is relatively novel for geological investigations, although contact orientations have been examined in the context of the mechanical behavior of granular materials (Nouguier-Lehon et al., 2003; Shodja and Nezami, 2003), work to date has been confined to modeling two-dimensional situations under biaxial loading. A reasonable interpretation of the data shown here is that a shear sense may be indicated. Because most or all garnet growth predated schistosity formation, it may be posed that they behaved like rigid bodies in a deforming medium, in which case a northeast-upwards, southeast-downwards shear would produce the observed pattern. Metamorphic conditions at Mica Dam did not reach temperatures sufficient to allow garnet to undergo plastic deformation, so the observed shape anisotropy is most likely a growth feature. In this interpretation, the alignment of long axes may have been caused by rotation during shearing. However, shape alteration due to brittle deformation or resorption cannot be ruled out based on these data.

QUANT3D was used to analyze the shape fabrics in quartz + plagioclase and garnet (Table 2; Fig. 9a–c). To ameliorate the effects of inhomogeneity, the analyses were done on a spherical subsample of the data that excluded the large quartz vein. For the quartzofeldspathic layers, the SVD 3D rose diagrams indicate that the foliation is stronger vertically than laterally. The view along the second fabric eigenvector (Fig. 9b) suggests a secondary fabric component about 5° counter-clockwise from the main fabric that matches the orientation of the shear sense in the garnet contact data. All three fabric tensors give similar results for principal directions (Table 2), while for the degree of anisotropy and shape indices they give different results reflecting their different calculations. The SVD component measurements are cubed relative to the SLD, which accentuates the influence of long measurements over short ones, giving rise to greater anisotropy and elongation. For this fabric the MIL and SLD give similar results.

Fabric analysis of the garnet (Fig. 9d–f) corroborates the general trends identified in the BLOB3D results, indicating shape anisotropy with a primary axis pointing predominantly vertically. Despite the very different character of the phases, the principal directions as measured by the SVD and SLD are very similar to those measured for quartz + plagioclase, suggesting that the garnets achieved their orientation during the development of the foliation. The SVD and SLD eigenvector orientations (Table 2) are also

Table 2
Grain shape fabric analysis results from Quant3D

	Quartz-Plagioclase			Garnet		
	SVD	SLD	MIL	SVD	SLD	MIL
\hat{u}_1	143°/87°	176°/87°	170°/85°	104°/76°	155°/85°	153°/53°
\hat{u}_2	320°/3°	321°/3°	324°/4°	312°/12°	329°/5°	29°/23°
\hat{u}_3	50°/0°	51°/2°	54°/2°	221°/6°	59/1°	287°/27°
DA	4.66	1.59	1.56	1.51	1.11	1.02
I	0.21	0.63	0.64	0.66	0.90	0.98
E	0.29	0.15	0.20	0.28	0.07	0.01

SVD: star volume distribution; SLD: star length distribution; MIL: mean intercept length; \hat{u}_1 , \hat{u}_2 , \hat{u}_3 : eigenvectors, trend and plunge. Other quantities based on eigenvalues $\hat{\tau}_1$, $\hat{\tau}_2$, $\hat{\tau}_3$; DA (degree of anisotropy): $\hat{\tau}_1/\hat{\tau}_3$; I (isotropy index): $\hat{\tau}_3/\hat{\tau}_1$; E (elongation index): $1 - \hat{\tau}_2/\hat{\tau}_1$.

similar to those obtained using the BLOB3D-derived long axes of individual garnets (Table 1), confirming that the volume-averaged approach implemented in QUANT3D achieves comparable results. The MIL method in this case detects virtually no shape anisotropy, rendering the eigenvector orientations meaningless. The absence of an anisotropy signal can be traced to the sparseness of garnet (about 7% of rock volume, vs. 40% for the quartzofeldspathic layers). Because MIL traverses cross multiple material boundaries, the method is sensitive to the spatial distribution of a sparse phase as well as shape; it essentially measures how many crystals are intersected in each orientation. These results illustrate the utility of employing multiple metrics, as each quantifies a different textural aspect of the rock volume.

5. Discussion

As demonstrated here, the applications of HRXCT range from three-dimensional visualization to quantitative textural analysis. Three-dimensional quantities such as fabric tensors and contact orientations that formerly had to be acquired relatively laboriously by examination of multiple orthogonal thin sections can now be routine. Typical scanning times for small samples (1" cores, thin section chips) are 1–2 h using current equipment based on microfocal X-ray sources, and larger specimens can typically be scanned in 2–6 h. The software analyses can take from minutes to several hours, depending on the type of data required. Both of these time requirements will continue to fall as scanning and computer technology advance, and

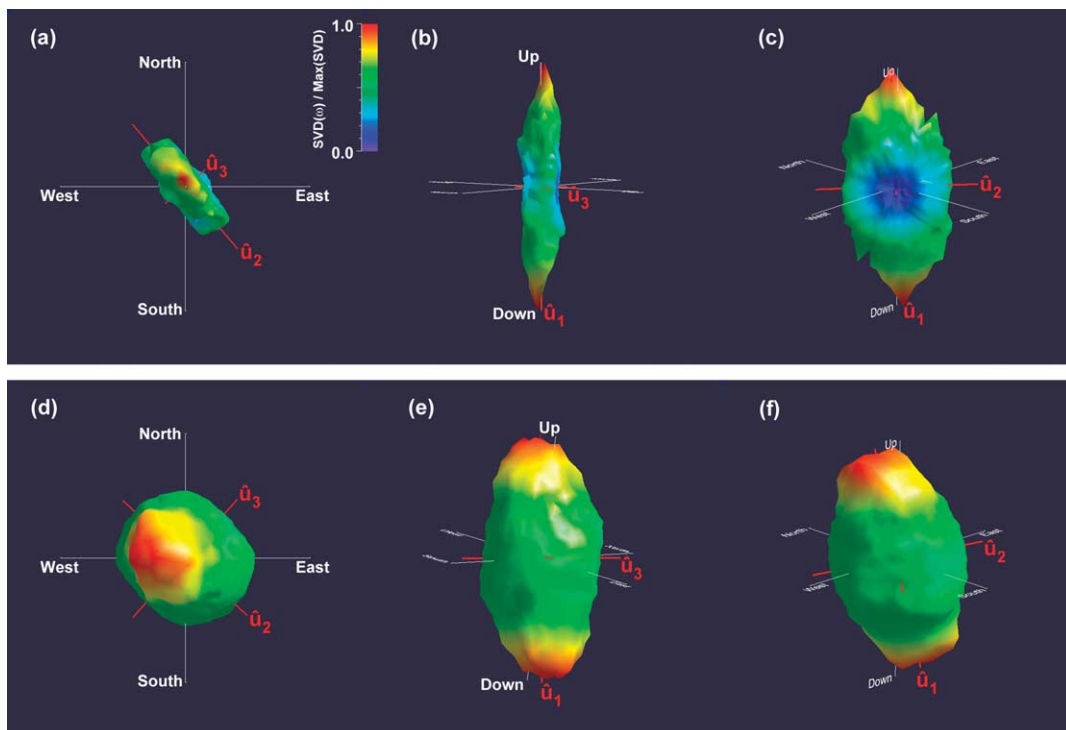


Fig. 9. 3D rose diagrams showing relative SVD component magnitudes for quartz + plagioclase (upper row) and garnet (lower row) in sample MD generated by QUANT3D. First diagram in each row (a,d) is viewed down the 'Up' axis; second diagram (b,e) is viewed along the second eigenvector, and third (c,f) is an arbitrary orientation. The diagrams are stored in VRML 97 format, and can be viewed interactively with a number of software applications and browser plug-ins.

with further software development. At the same time, it should be emphasized that this work does not replace traditional petrographic observation; indeed, thin section examination will often be crucial for correctly determining mineralogy to direct scan data segmentation.

Scanning can have further ancillary benefits for working with geological specimens. Using scan data it is straightforward to determine if a thin section cut afterwards contains the central section of a particular crystal for chemical or isotopic analysis. Similarly, scan data can also provide information on the choice of where sections should be cut, and after cutting the investigator retains information for what is above and/or below the plane.

All the software discussed here was developed in the IDL (Interactive Data Language; Research Systems, Inc., Boulder, CO) programming environment. The programs can be run using either a full IDL license or with the freely available IDL “Virtual Machine”. They can be run on most computer platforms (Windows, Macintosh, Linux, Unix).

Acknowledgements

This research and software development was supported in part by the National Science Foundation (grant EAR-0113480). BLOB3D processing was done by Charna Meth. The manuscript was improved thanks to thorough reviews by G.E. Lloyd and K. Ullemeyer.

Appendix A. Fabric tensor and moment of inertia calculation

A continuous quantity that varies with orientation (e.g. SVD, SLD, MIL) can be summarized using a fabric tensor based on the moment of inertia, following standard procedures for directional data (e.g. Watson, 1966; Mardia and Jupp, 2000), extended by Karlsson and Cruz-Orive (1993). The data consist of a set of n measurements, with each measurement i considered as a vector \mathbf{a}_i with orientation defined by spherical coordinates (θ_i, ϕ_i) and magnitude $|\mathbf{a}_i|$ equal to the measured value in that orientation:

$$\mathbf{a}_i = \begin{pmatrix} a_{xi} \\ a_{yi} \\ a_{zi} \end{pmatrix} = \begin{pmatrix} |\mathbf{a}_i| \sin \theta_i \cos \phi_i \\ |\mathbf{a}_i| \sin \theta_i \sin \phi_i \\ |\mathbf{a}_i| \cos \theta_i \end{pmatrix}.$$

Given an axis of arbitrary direction \mathbf{u} the moment of inertia $I(\mathbf{u})$ is the sum of the squared distance from each vector to \mathbf{u}

$$I(\mathbf{u}) = \sum_{i=1}^n |\mathbf{a}_i|^2 - \mathbf{u}^T \mathbf{T} \mathbf{u},$$

where \mathbf{T} is the orientation matrix:

$$\mathbf{T} = \sum_{i=1}^n \mathbf{a}_i \mathbf{a}_i^T = \begin{bmatrix} \sum_{i=1}^n a_{xi}^2 & \sum_{i=1}^n a_{xi} a_{yi} & \sum_{i=1}^n a_{xi} a_{zi} \\ \sum_{i=1}^n a_{xi} a_{yi} & \sum_{i=1}^n a_{yi}^2 & \sum_{i=1}^n a_{yi} a_{zi} \\ \sum_{i=1}^n a_{xi} a_{zi} & \sum_{i=1}^n a_{yi} a_{zi} & \sum_{i=1}^n a_{zi}^2 \end{bmatrix}.$$

We denote the three eigenvalues of \mathbf{T} as $\hat{\tau}_1 > \hat{\tau}_2 > \hat{\tau}_3$ and their corresponding eigenvectors as $\hat{\mathbf{u}}_1, \hat{\mathbf{u}}_2, \hat{\mathbf{u}}_3$ (This numbering convention stems from Odgaard et al. (1997), and it should be noted that it is opposite in some other works; for example, Karlsson and Cruz-Orive (1993) and Mardia and Jupp (2000) assign the lowest eigenvalue to $\hat{\tau}_1$ rather than the highest.) All variables include hat symbols to emphasize that they are estimates of the true underlying quantities. It can be shown that $\hat{\mathbf{u}}_1$ is the direction in which the moment of inertia is minimized, and $\hat{\mathbf{u}}_3$ is the maximum (Mardia and Jupp, 2000). The moment of inertia for each axis is equal to the sum of the eigenvalues for the other two (Karlsson and Cruz-Orive, 1993).

To allow comparison among different samples and analyses, the fabric tensor \mathbf{F} is defined as the orientation matrix normalized by the sum of its eigenvalues (Odgaard et al., 1997):

$$\mathbf{F} = \mathbf{T} / \sum_{i=1}^3 \hat{\tau}_i.$$

References

- Benn, D.I., 1994. Fabric shape and the interpretation of sedimentary fabric data. *Journal of Sedimentary Research, Section A: Sedimentary Petrology and Processes* A64, 910–915.
- Brown, M.A., Brown, M., Carlson, W.D., Denison, C., 1999. Topology of syntectonic melt flow networks in the deep crust: inferences from three-dimensional images of leucosome geometry in migmatites. *American Mineralogist* 84, 1793–1818.
- Carlson, W.D., Denison, C., 1992. Mechanisms of porphyroblast crystallization: results from high-resolution computed X-ray tomography. *Science* 257, 1236–1239.
- Carlson, W.D., Denison, C., Ketcham, R.A., 1995. Controls on the nucleation and growth of porphyroblasts: kinetics from natural textures and numerical models. *Geological Journal* 30, 207–225.
- Cowin, S.C., 1986. Wolff's law of trabecular architecture at remodeling equilibrium. *Journal of Biomedical Engineering* 108, 83–88.
- Crowley, J.L., Ghent, E.D., Carr, S.D., Simony, P.S., Hamilton, M.A., 2000. Multiple thermotectonic events in a continuous metamorphic sequence, Mica Creek area, southeastern Canadian Cordillera. *Geological Materials Research*, 2.
- Cruz-Orive, L.M., Karlsson, L.M., Larsen, S.E., Wainschtein, F., 1992. Characterizing anisotropy: a new concept. *Micron Microscopica Acta* 23, 75–76.
- Denison, C., Carlson, W.D., 1997. Three-dimensional quantitative textural

- analysis of metamorphic rocks using high-resolution computed X-ray tomography: Part II. Application to natural samples. *Journal of Metamorphic Geology* 15, 45–57.
- Denison, C., Carlson, W.D., Ketcham, R.A., 1997. Three-dimensional quantitative textural analysis of metamorphic rocks using high-resolution computed X-ray tomography; Part I. Methods and techniques. *Journal of Metamorphic Geology* 15, 29–44.
- Fajardo, R.J., Müller, R., 2001. Three-dimensional analysis of nonhuman primate trabecular architecture using micro-computed tomography. *American Journal of Physical Anthropology* 115, 327–336.
- Grégoire, V., Darrozes, J., Gaillot, P., Nédélec, A., Launeau, P., 1998. Magnetite grain shape fabric and distribution anisotropy vs. rock magnetic fabric: a three-dimensional case study. *Journal of Structural Geology* 20, 937–944.
- Harrigan, T.P., Mann, R.W., 1984. Characterization of microstructural anisotropy in orthotropic materials using a second rank tensor. *Journal of Materials Science* 19, 761–767.
- Hirsch, D.M., Ketcham, R.A., Carlson, W.D., 2000. An evaluation of spatial correlation functions in textural analysis of metamorphic rocks. *Geological Materials Research*, 2.
- Karlsson, L.M., Cruz-Orive, L.M., 1993. Characterizing structural anisotropy using the star volume distribution. In: *Stereology in Materials Science: Demonstration of Some Methods*. Unpublished PhD thesis, Royal Institute of Technology, Stockholm.
- Ketcham, R.A., Carlson, W.D., 2001. Acquisition, optimization and interpretation of X-ray computed tomographic imagery: applications to the geosciences. *Computers and Geosciences* 27, 381–400.
- Ketcham, R.A., Ryan, T., 2004. Quantification and visualization of anisotropy in trabecular bone. *Journal of Microscopy* 213, 158–171.
- Ketcham, R.A., in press. Computational methods for quantitative analysis of three-dimensional features in geological specimens. *Geosphere*, in press.
- Koerberl, C., Denison, C., Ketcham, R.A., Reimold, W.U., 2002. High resolution X-ray computed tomography of impactites. *Journal of Geophysical Research—Planets* 107, 5089. doi:10.1029/2001JE001833.
- Launeau, P., Robin, P.-Y.F., 1996. Fabric analysis using the intercept method. *Tectonophysics* 267, 91–119.
- Mardia, K.V., Jupp, P.E., 2000. *Directional Statistics*. Wiley, Chichester.
- Markowicz, A.A., 1993. X-ray physics. In: Van Grieken, R.E., Markowicz, A.A. (Eds.), *Handbook of X-ray Spectrometry Practical Spectroscopy*, vol. 14. Marcel Dekker, New York, pp. 1–28.
- McCullough, E.C., 1975. Photon attenuation in computed tomography. *Medical Physics* 2, 307–320.
- Nouguier-Lehon, C., Cambou, B., Vincens, E., 2003. Influence of particle shape and angularity on the behaviour of granular materials: a numerical analysis. *International Journal for Numerical and Analytical Methods in Geomechanics* 27, 1207–1226.
- Odgaard, A., Kabel, J., van Rietbergen, B., Dalstra, M., Huiskes, R., 1997. Fabric and elastic principle directions of cancellous bone are closely related. *Journal of Biomechanics* 30, 487–495.
- Panozzo, R.H., 1983. Two-dimensional analysis of shape-fabric using projections of digitized lines in a plane. *Tectonophysics* 95, 279–294.
- Panozzo Heilbronner, R., 1992. The autocorrelation function: an image processing tool for fabric analysis. *Tectonophysics* 212, 351–370.
- Philpotts, A.R., Brustman, C.M., Shi, J., Carlson, W.D., Denison, C., 1999. Plagioclase-chain networks in slowly cooled basaltic magma. *American Mineralogist* 84, 1819–1829.
- Rink, M., 1976. A computerized quantitative image analysis procedure for investigating images and an adapted image process. *Journal of Microscopy* 107, 267–286.
- Ryan, T.M., Ketcham, R.A., 2002. The three-dimensional structure of trabecular bone in the femoral head of strepsirrhine primates. *Journal of Human Evolution* 43, 1–26.
- Sahagian, D., Proussevitch, A., Carlson, W.D., 2002. Timing of Colorado Plateau uplift: Initial constraints from vesicular basalt-derived paleoelevations. *Geology* 30, 807–810.
- Shimamoto, T., Ikeda, Y., 1976. A simple algebraic method for strain estimation from deformed ellipsoidal objects; 1. Basic theory. *Tectonophysics* 36, 315–337.
- Shodja, H.M., Nezami, E.G., 2003. A micromechanical study of rolling and sliding contacts in assemblies of oval granules. *International Journal for Numerical and Analytical Methods in Geomechanics* 27, 403–424.
- Simony, P.S., Ghent, E.D., Craw, D., Mitchell, W., Robbins, D.B., 1980. Structural and metamorphic evolution of northeast flank of Shuswap complex, southern Canoe River area, British Columbia. *Geological Society of America Memoir* 153, 445–461.
- Smit, T.H., Schneider, E., Odgaard, A., 1998. Star length distribution: a volume-based concept for the characterization of structural anisotropy. *Journal of Microscopy* 191, 249–257.
- Tinkham, D.K., Ghent, E.D., 2003. Estimating garnet growth P–T conditions with pseudosections and the problem of effective bulk composition. *GACMAC Annual Meeting Abstracts*, 28.
- Van Geet, M., Swennen, R., Wevers, M., 2000. Quantitative analysis of reservoir rocks by microfocus X-ray computerised tomography. *Sedimentary Geology* 132, 25–36.
- Watson, G.S., 1966. The statistics of orientation data. *Journal of Geology* 74, 786–797.
- Whitehouse, W.J., 1974. The quantitative morphology of anisotropic trabecular bone. *Journal of Microscopy* 101, 153–168.